RESEARCH ARTICLE

ADVANCED SENSOR RESEARCH Open Access

www.advsensorres.com

Electrospun Vanadium Pentoxide (V_2O_5) Nanofibers for Enhanced Humidity Sensing

Hankun Yang, Monsur Islam, Vanessa Trouillet, Martin Sommer, Jan G. Korvink, Uli Lemmer, and Bharat Sharma**

Adequate humidity monitoring is crucial for many industrial and consumer applications. Among various moisture-absorbing materials, 2D materials are potential contestants for fabricating humidity sensors owing to their fascinating ultra-high surface-to-volume ratio, abundant active sites, and large carrier mobilities. In this work, vanadium pentoxide (V_2O_5) nanofibers (NFs) produced by a facile electrospinning method using VO(acac)2 10% Polyacrylonitrile/Dimethylformamid are showcased for humidity sensing. The annealing temperature-dependent (400–600 °C) variations in morphology and composition of the electrospun V_2O_5 NFs are studied by structural and physicochemical characterization methods. Subsequently, the V_2O_5 NFs are effectively used for humidity sensing at room temperature (RT). It is demonstrated that the optimum RT humidity response and sensitivity of the NF sensor are obtained at an annealing temperature of 500 °C with a high surface area of 14.8 m^2g^{-1} containing large porous fibers ranging from 200 to 500 nm diameter. The synthesized V_2O_5 NF sensor exhibits high sensitivity to water at RT (max. 1.427 at 90 %RH), excellent linearity, wide range (10–90%RH), and quick response and recovery times. This work sets a benchmark for designing novel V_2O_5-based RT humidity sensing devices.

1. Introduction

The accurate control of moisture content in the air is essential for widespread applications, such as in the biomedical and chemical fields, as well as in healthcare, automobile, mining, agriculture, and food processing.[1–6] The market for humidity sensors is growing rapidly in a range of applications, driven by the constant quest for optimizing their performance and the strong desire to enhance the living standard of human beings.[7] The mammoth demand for humidifiers and humidity monitoring equipment has fueled the development of portable, reliable, energy-saving, and superior-quality humidity sensors.[8] These advancements in humidity sensors encompass tailored transducer characteristics, including sensing elements, structure, design, transduction principles, and material processing technologies.[1,3] In this scenario, new sensitive elements are the key players in ensuring the state-of-the-art performance of these humidity sensors. Multiple sensing mechanisms exist today, which can be categorized into electrical (capacitive, chemiresistive, and field-effect-based), mechanical (surface acoustic wave, and quartz crystal microbalance), and optical (colorimetric, fluorescence, and polarization/absorbance). Among these, the chemiresistive principle stands out as the most simple and inexpensive yet still reliable and thus widespread mechanism with many commercial applications.[9] For chemiresistive humidity sensors, a wide range of sensitive materials has been explored, including metal oxides (MOX), polymers, carbon nanomaterials, and inorganic/organic hybrids.[10–13] These materials have a variety of appealing properties for humidity sensors, but they also have some unavoidable drawbacks that have prevented their use in real-world applications. For instance, ceramic oxides frequently have high levels of hysteresis, low sensitivity, long response and recovery times, and certain toxicity levels.[14] Similarly, carbon nanomaterials exhibit low selectivity, poor reproducibility, and possible long-term drifts in response. Organic and polymeric materials suffer from several issues, which are mostly related to hysteresis changes, low degree of sensitivity at low humidity, and water solubility at high humidity levels.[10–15] Nevertheless, some organic materials show exceptional sensitivity at high humidity and fast response and recovery time.[15] Still, they are less performant at lower humidity values.

H. Yang, M. Islam, M. Sommer, J. G. Korvink, U. Lemmer, B. Sharma
Institute of Microstructure Technology (IMT)
Karlsruhe Institute of Technology (KIT)
76344 Eggenstein-Leopoldshafen, Germany
E-mail: uli.lemmer@kit.edu; bharat.sharma@kit.edu

H. Yang, U. Lemmer
Light Technology Institute (LTI)
Karlsruhe Institute of Technology (KIT)
76131 Karlsruhe, Germany

V. Trouillet
Institute for Applied Materials (IAM-ESS) and Karlsruhe Nano Micro Facility (KNMFi)
Karlsruhe Institute of Technology (KIT)
Hermann-von-Helmholtz-Platz 1, 76344 Eggenstein-Leopoldshafen, Germany

The ORCID identification number(s) for the author(s) of this article can be found under https://doi.org/10.1002/adsr.202500040

DOI: 10.1002/adsr.202500040

Surface modification with noble metal (Pd or Pt) has been tried to catalyze the removal of hydroxyl ions and enhance the humidity response.[16–18] Other MOX species, such as NiO, CuO, as well as Al_2O_3 can be used to capture hydroxyls and supply oxygen adsorption sites.[19–21] However, all these modifications lead to poor performance in the low humidity range (0 – 20%RH). The addition of hydrophobic coatings such as polydimethylsiloxane (PDMS) can reasonably improve the humidity resistance. Still, the hydrophobic layer negatively impedes the efficient permeation of water molecules and hampers the MOX surface activity, causing a loss in sensitivity.[22] Recent advancements in zeolites, mesoporous organics, or metalorganic frameworks (MOFs) could offer a "breathable" membrane support and solve these issues. However, the target molecules would diffuse through the porous structures and have negligible impact on the activity of the MOXs.[23–27] In addition, the selective permeation of target molecules could be ensured by tailoring their pore sizes or surface modification.

In contrast to conventional humidity sensing materials, advanced nanostructured humidity sensors are mostly limited to nanowires, nanofibers (NFs), and nanoparticles (NPs).[28–30] Amongst a diverse range of nanostructures, 1D materials such as nanorods, nanoribbons, nanowires, nanotubes, and nanofibers have sparked the materials research community due to their distinctive properties resulting from quantum and surface effects.[31] 1D nanostructures have become popular as ideal elements for the upcoming class of effective humidity sensors. Meanwhile, 1D nanomaterials are novel candidates for high-performance sensors due to their ultra-high specific surface area, high carrier mobility, and superior catalytic activities. Amongst other nanostructures, NFs are equally well-suited for these kinds of functional applications because of their high surface-to-volume ratios.[6–8] The development of novel gas sensors prepared from suitable NF materials has been motivated by the leading MOX candidates.[32,33] However, the use of MOX-NF gas sensors has been restricted to the detection of highly reactive analytes necessitating operation at high temperatures or reactivation by UV irradiation.[34,35]

In this context, transition semiconductor metal oxides (TMOX) based thin film chemiresistors have been developed.[36] TMOX offers low-cost, compact, and promising device configurations for widespread applications.[37–39] Especially, TMOX with d0 electronic configurations, such as V_2O_5, attracted considerable attention in the past owing to its layered structure for abundant adsorption of gaseous molecules and catalyzing reactions.[37–39] The layered V_2O_5 is thermodynamically the most stable oxide with an optical band gap of 2.3 eV as compared with other oxides of vanadium for various technological applications in batteries, bolometers, electrochromic/photochromic displays, and photovoltaic electrodes.[40–45] As an n-type TMOX, whose electronic conductivity rises when the V^{5+} species are reduced to V^{4+} when exposed to reducing gases.[46] At RT, the electronic conductivity of the as-prepared V_2O_5 NF is of the order of 0.5 S cm^{-1}.[47] It is noteworthy that the performance of UV-irradiated or thermally activated devices degrades over long-term exposure to UV light or high temperatures.[48,49] Moreover, the absorption in the UV range restricts the diverse industrial usage of the sensor.[30,50]

Tadeo et al. reported the use of ultrasonically nebulized V_2O_5 thin films to successfully measure relative humidity ranging from 25% to 76%RH.[51] Pawar et al. used V_2O_5 nanosheets to measure relative humidity for a wider range from 4% to 97.3%RH.[52] But this sensor lacked linearity. Furthermore, the signal is plagued with high noise, and thereby a low detection limit could not be achieved. Charlotte and Viannie used V_2O_5 nanoparticles for humidity sensing.[53] The sensor showed exceptional response and recovery time of 60 and 21s. Very recently, Cho et al. used directly deposited V_2O_5 nanobelts using an O_2-assisted physical vapor transport method.[54] The sensor showed sensitivity toward various gases besides relative humidity.

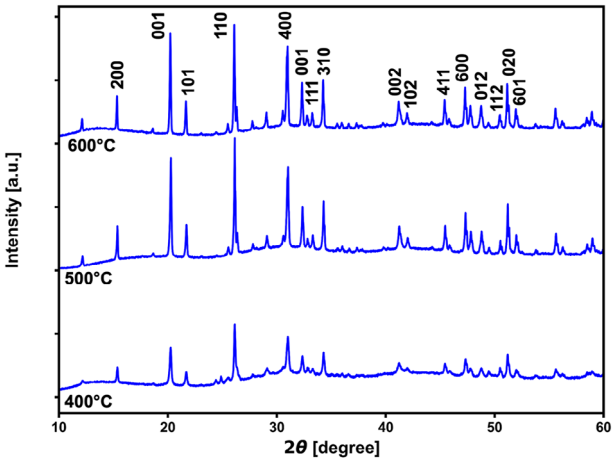

Figure 1. XRD patterns of V_2O_5 NFs annealed at different temperatures.

Electrospinning is an interesting method of manufacturing porous nanofibers. This method involves pushing a precursor polymer solution at a predefined flow rate through a nozzle. When a high voltage is applied between the nozzle and the target, a Taylor cone forms at the tip of the nozzle. Subsequently, a precursor stream with an even smaller diameter is ejected to the target. The collected precursor material at the target is then annealed. Electrospinning is an inexpensive and versatile method to create fiber structures with hierarchical porosity, including nano- and mesopores. [32] Therefore, electrospinning is a well-suited method to create nanomaterials for humidity sensing applications due to their high surface-to-volume ratio. In this work, we first analyze electrospun V_2O_5 nanofibers that are annealed at different temperatures and assess their performance for RT humidity sensing.

2. Results and Discussion

2.1. Structural and Morphological Studies

The XRD patterns of V_2O_5 NFs annealed at 400–600 °C are shown in (**Figure 1**). The V_2O_5 NFs annealed at 400 °C displayed less intense (200), (001), (110), and (400) peaks for V_2O_5 planes. In contrast, the annealed V_2O_5 NFs at 500 and 600 °C revealed an increase in the intensity of the planes, signifying the high crystallinity of these samples. The maximum intensity peaks at 2θ = 20.32° and 26.4° show growth for the (001) and (110) orientations of polycrystalline grains at 600 °C. All diffraction peaks were assigned to the orthorhombic V_2O_5 crystal system Pmmn space group (JCPDS # 77–2418).[65] The optimized annealing tempera-

Table 1. a) Crystallite size, lattice constants, and volume of the unit cell of V_2O_5 NFs. b) Rietveld Analysis Fitting Parameters. c) BET Results.

T [°C]	D [nm]	A [Å]	b [Å]	c [Å]	V [Å^3]	δ [10^{-3} lines nm^{-2}]
400	115	11.5158	3.5667	4.3803	179.9138	5.26×10^{-3}
500	95	11.5143	3.5649	4.3747	179.5697	2.65×10^{-3}
600	107	11.5148	3.5654	4.3753	179.6273	3.93×10^{-3}

b) Rietveld Analysis Fitting Parameters

T [°C]	GOF	R_{exp}	R_{wp}	R_p	Weighted Durbin Watson
400	1.93	1.99	3.84	2.91	0.69
500	3.02	2.05	6.18	3.86	0.49
600	2.85	2.12	6.03	4.45	0.49

c) BET Results

T [°C]	Mean pore diameter [nm]	Total pore volume [cm^3 g^{-1}]	BET surface area [m^2 g^{-1}]
400	22.901	0.0743	12.992
500	19.688	0.0728	14.811
600	12.173	0.0502	16.507

ture of 500 °C was fixed for V_2O_5 NFs with maximum local crystallinity. No other characteristic impurity or secondary vanadium peaks affirm the high purity of synthesized V_2O_5 NFs.

The average crystallite size of these V_2O_5 NFs estimated by the Halder-Wagner method implemented in the PDXL program was between 90 and 100 nm. In addition, the lattice refinement by the Rietveld method (Figure S3, Supporting Information) matches perfectly the crystal lattice parameters of the V_2O_5 phase. The crystallite size obtained from the Rietveld method indicated 95 to 107 nm growth from 500 to 600 °C. The crystallite size results were comparable with those obtained by the Halder-Wagner method. The unit cell parameters determined from the PDXL program, as listed in **Table 1**, are consistent with the three standard cell parameters of V_2O_5: $a_0 = 11.516$ Å, $b_0 = 3.5656$ Å, $c_0 = 4.3727$ Å, and $V_0 = 179.55$ Å^3.[66]

According to the formula $\delta = \frac{1}{D^2}$,[67,68] where D is the crystallite size ($D = \frac{K\lambda}{\sqrt{\beta^2 - \beta'^2}\cos\theta}$, $K = 0.9$,[69] 2θ = Bragg's angle, β = full width at half maxima peak, and β' = instrumental correction of broadening with a standard silicon disc;[70] the dislocation densities of V_2O_5 NFs were estimated (Table 1). The small δ for a temperature of 500 °C confirms the excellent local crystallinity of V_2O_5 NFs for this annealing condition.[67]

The V_2O_5 NFs N_2 adsorption and desorption isotherms are illustrated in supplementary Figure S4 (Supporting Information). According to the IUPAC classification, the samples exhibit type II behavior, suggesting an evolution of macroporous V_2O_5 NFs.[71] A Brunauer-Emmett-Teller (BET) surface area of 14.811 m^2 g^{-1} was observed at 500 °C, compared to the BET surface area of 12.992 m^2 g^{-1} at 400 °C as depicted in Figure S4a,b, Supporting Information). At 600 °C, V_2O_5 NFs had the maximum surface area of 16.507 m^2 g^{-1} among all the samples (Figure S4c, Supporting Information). The narrow adsorption-desorption hysteresis plots at different relative pressures are characteristics of hierarchical porosity.[72] The pore size distributions are also presented in Figure S4d (Supporting Information) for comparison. Additionally, the quick uptake ($P/P_0 > 0.9$) at 600 °C indicates large pores. These properties of our V_2O_5 NFs are highly promising for absorbing high amounts of water vapor.

The morphology of the electrospun V_2O_5 NFs was characterized by electron microscopy (**Figure 2**). The SEM image of the electrospun V_2O_5 NFs reveals a non-uniform 1D nanofibrous structure (Figure 2a). A close view of Figure 2b indicates the porous, hollow, and irregularly shaped fibers. The diameter of the fibers could not be recognized well; however, the size of the minimum to the maximum thickness of the fiber envelope varied from 150 to 110 nm with irregular surfaces. At high resolution, the morphology of fibers is slightly porous and flaky (Figure 2c), which may be due to the presence of partially melted PAN on the surfaces and the incomplete crystallization of the fibers at this temperature. Beyond 400 °C, PAN may disintegrate completely,[73] and the high annealing temperature facilitates the crystal growth of fibers along the preferred orientations (001) and (110) planes, as demonstrated by the XRD results. The fibrous morphology is still maintained after annealing at 500 °C, as shown in Figure 2d, but a notable uniformity in the length and shape of NFs is seen. The fibers shrunk in diameter to 200–500 nm and most of the fibers grew with protruded surfaces (Figure 2e). However, there were many pores on the rod-like surface with diameters of ≈50–80 nm. This might be caused by the polymer expansion and outgassing during heat treatment (Figure 2f). As shown in Figure 2g, the fibers produced with an annealing temperature of 600 °C have a particle-like and globular structure at low resolution with a diameter of 200–1150 nm, primarily because of the rapid growth of crystal size of V_2O_5 NFs after crystallization (**Figure 3**h,i).

These SEM findings suggest that the morphology of the electrospun V_2O_5 NFs could be well controlled by adjusting the annealing procedure, thereby tailoring the pore size and BET surface areas. Thus, the V_2O_5 NFs can be made suitable for gas sensing applications.

TEM analysis was performed to gain more understanding of the morphology and structure of the V_2O_5 NFs at high resolution (Figure 3). At 400 °C, the V_2O_5 NFs are hollow, porous, and randomly oriented, in agreement with the SEM findings (Figure 3a–d). The TEM images at high resolution further confirm the hollow nature of these NFs (Figure 3b) with some protrusions and pores over the surfaces demonstrating partial crystallinity with crystals as small as 80 nm. The HRTEM images show the presence of different orientations of planes (200) and (001) corresponding to the interplanar spacing of 0.58 nm and 0.71 nm (Figure 3c,d). The surface of the NFs is discontinuous and twisted, which confirms the irregular morphology of NFs at such a low temperature. The SAD pattern shows diffused spot patterns indicating the presence of randomly oriented fibers (inset Figure 3d). As the temperature increased to 500 °C, the fibrous morphology became more regular, and the hollow fibers turned denser and compactly oriented along (110) planes (Figure 3e–h). These images highlight the significance of temperature optimization for achieving a fibrous morphology. Furthermore, PAN, which serves as the template for the fiber microstructure, apparently disintegrates at >400 °C.[73] Additionally, the disintegration of the NFs architecture is facilitated by the rapid growth of V_2O_5 crystals at >500 °C (Figure 3i–l). Lattice

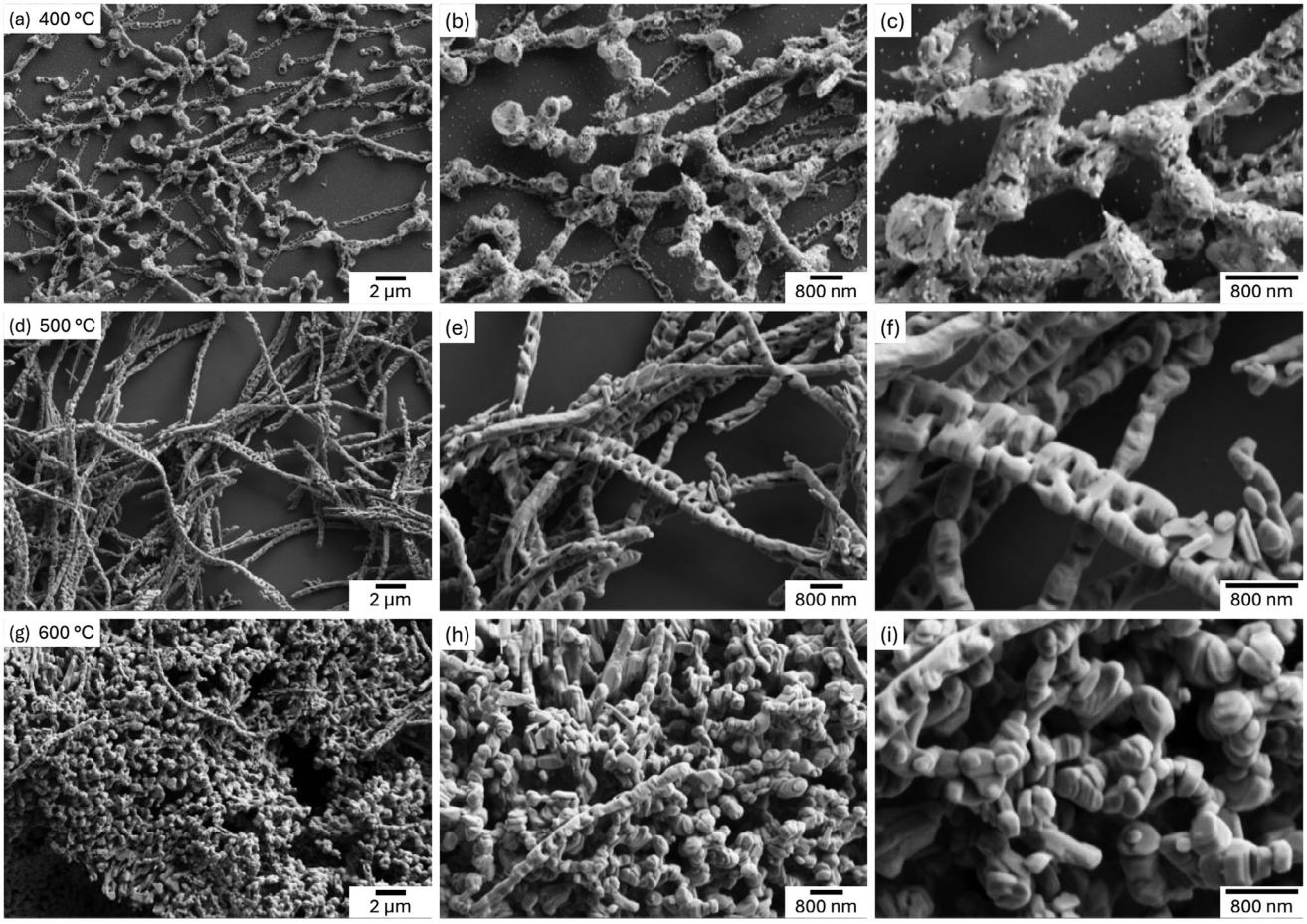

Figure 2. Surface morphology of V_2O_5 NFs at different annealing temperatures. a-c) 400 °C, d–f) 500 °C, and g–i) 600 °C.

fringes with a d-spacing of 0.26 nm were visible in the HRTEM bright field imaging of samples annealed at 500 and 600 °C, which agrees well with the d-spacing of the (110) V_2O_5 (JCPDS card no. 41–1426; Figure 3h,l). These results also support the XRD findings, which confirm the orientations of V_2O_5 along (001) and (110) planes.[51] The SAD patterns shown in the inset of Figure 3h,l shows the increased crystallinity and growth of V_2O_5 NFs with temperature.

The compositional TEM mapping analysis of V_2O_5 fibers at 400–500 °C is shown in Figure S5a–c (Supporting Information). The representative EDS spectrum at the bottom of each map shows the uniformity in the composition of V_2O_5 NFs. Crystalline coarsening with higher temperatures is shown with hollow tubes only for the 400 °C sample. The samples annealed at 500 and 600 °C collapse into coarse globules while maintaining the fiber form. A low concentration (<1%) of Na was found over the fiber surfaces. It has been reported that the number of impurities depends on the annealing temperature and geometry of the respective NFs.[73,74]

Additional information on the V_2O_5 NFs was obtained by XPS. The survey spectra of V_2O_5 NFs annealed at 400–600 °C are shown in Figure S6 (Supporting Information) and reveal the presence of V and O elements in all analyzed V_2O_5 NFs accompanied by some carbon species. The high-resolution core level O 1s and V 2p spectra of V_2O_5 NFs (**Figure 4**) allow the identification of the chemical states and chemical environment of V and O at the surface. The V 2p doublet with V $2p_{3/2}$ at 517.7 eV proves the presence of vanadium oxide, mainly as V_2O_5.[23,75–77] A further weak peak at 516.2 eV shows the presence of VO_2. The V 2p doublets are accompanied by the corresponding O 1s signal at 530.4 eV, attributed to lattice oxygen. Additionally, two O 1s contributions can be explained by the presence of some oxidized carbons (C═O and C—O). No further chemical states of vanadium were found, confirming high-quality V_2O_5 NFs in samples annealed at 500–600 °C (Figures S6, S7, Supporting Information; Figure 4).

As shown in Figure 4 and from the calculation of the atomic concentrations, the fibers annealed at 400 °C tend to contain a higher fraction of V^{4+} than the ones annealed at 500 and 600 °C. Given that the initial oxidation state of vanadium in $VO(acac)_2$ is V^{5+}, a high fraction of V^{4+} at 400 °C may be associated with the reducing power of the used organic precursors in the electrospun $VO(acac)_2$/PAN fibers.[78,79] Nevertheless, appropriate annealing conditions must be selected to discern the reduction action of each organic compound. The rise in the annealing temperature up to 500 and 600 °C tends to enhance the proportion of V^{5+}, such that fibers with smaller V^{4+}/V^{5+} ratios are obtained in a proportion of ≈1/17. Simultaneously, the ratio O(530.4 eV) / V_{total} also tends to increase slightly from 2.2 up to 2.4 sup-

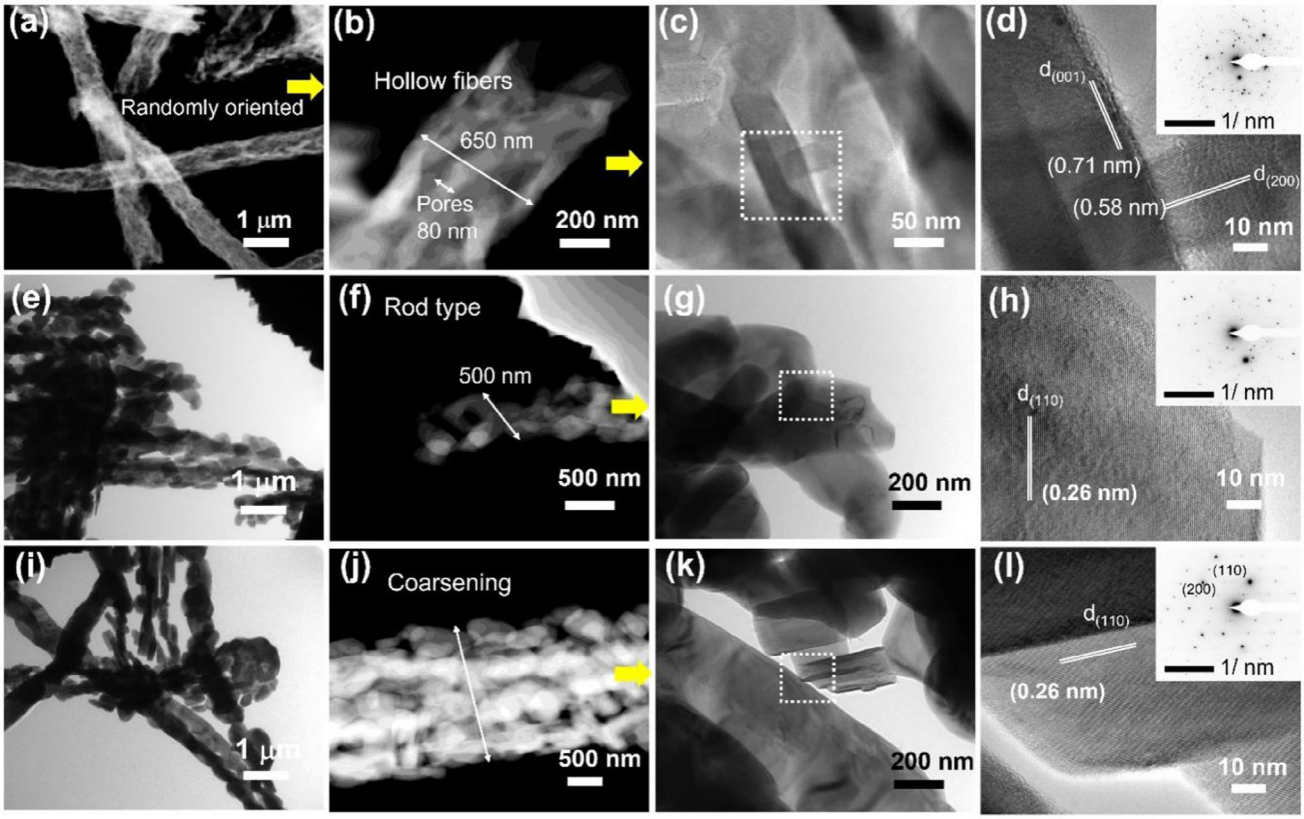

Figure 3. TEM images of V_2O_5 NFs at different annealing temperatures. a–d) 400 °C, e–h) 500 °C, and i–l) 600 °C. The inset shows corresponding SAD patterns.

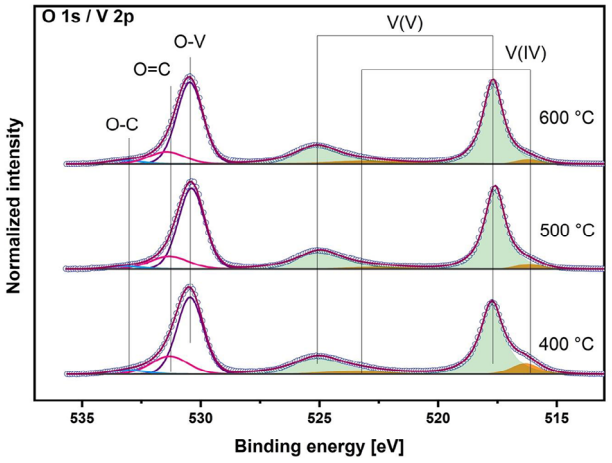

Figure 4. Normalized O 1s and V 2p core level spectra.

porting the presence of more V_2O_5 at higher annealing temperatures. Additionally, the contribution of the lattice oxygen peak increases slightly with temperature and nearly reaches the stoichiometric oxygen concentration at 600 °C based on the measured V^{4+} and V^{5+} concentrations. This finding indicates a trend of reduction of oxygen vacancies with increasing temperature. A straightforward interpretation of O 1s proving the presence of oxygen vacancies is hindered by several factors, like the presence of surface contamination or the possible presence of some hydroxides.[80,81]

Residual impurities of C and N were also found on the surface of all the annealed samples (Figure 4; Figures S6, S7, Supporting Information) as also evidenced by TEM findings. These species were assigned to partially reacted PAN or $VO(acac)_2$ and could affect the properties of the V_2O_5 NFs.[82]

2.2. Humidity Sensing

The reference resistance values (at 0%RH)) of the V_2O_5-based sensors annealed at varying temperatures are depicted in Figure S8 (Supporting Information). As the annealing temperature increases from 400 to 500 °C, the average resistance decreases from 0.37 to 0.23 MΩ. The higher electrical resistance is caused by incomplete crystallization, as discussed in Section 3.1. No significant change of resistance occurs by further increasing the annealing temperature to 600 °C.

Surprisingly, the sensing behavior also depends on the annealing temperature, as depicted in **Figure 5**. At 400 °C, the response from 30% to 90%RH is characterized by an initial spike in resistance followed by a gradual decline back to the reference level. A similar sensing behavior has been reported,[83] which further indicates the presence of VO_2 at 400 °C in the incompletely crystallized NFs. At 400 °C, a conventional response behavior can only be observed for the 10%RH. Thus,

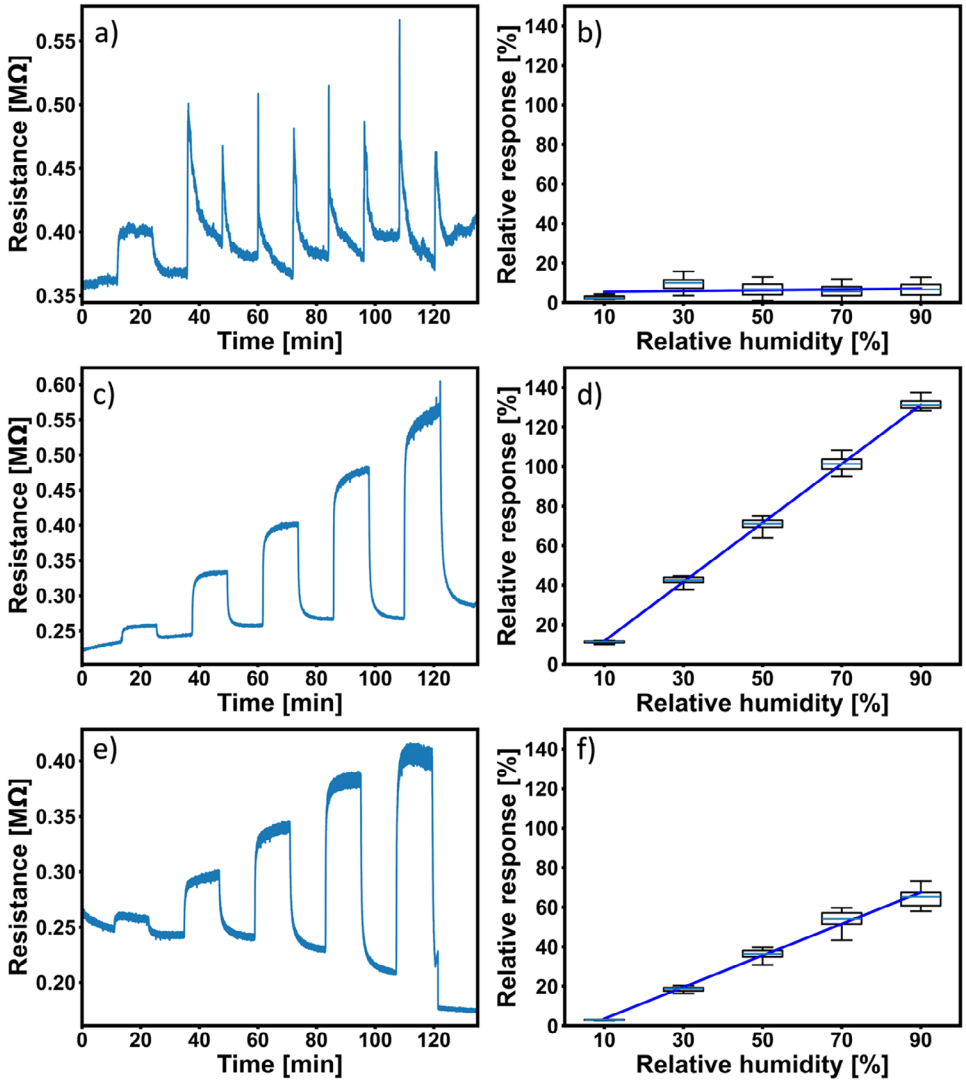

Figure 5. Sensitivity analysis of electrospun V_2O_5 NF annealed at different temperatures. a,c,e): median resistance data of the humidity measurement 400, 500, and 600 °C. b, d, f): relative response at 400, 500, and 600 °C.

400 °C samples are disregarded for further investigations in this research.

Samples annealed at 500 and 600 °C, exhibit a more conventional and stable sensing behavior across all measured humidity levels, as shown in Figure 5. In addition to the findings of the XRD and XPS analysis (Section 3.1), this further indicates that the V^{4+}/V^{5+} ratio decreases compared to the 400 °C samples. At both temperatures, 500 and 600 °C, the relative response correlates positively and highly linearly with RH. Because of the high linearity of the humidity-dependent relative response %RR(%RH), the calibration curve is fit by linear regression (according to Section S1.3, Supporting Information). The average calibration curve is shown in Figure 5 b, d, f while the derived sensitivity distribution for all subsensors and for an annealing temperature of 500 and 600 °C are shown in Figure S9a, Supporting Information). At 500 °C, the majority of sub-sensors achieve a sensitivity between 1.3 and 1.4, with the maximum at 1.427. For an annealing temperature of 600 °C, the average sensitivity of the subsensors is lower and is calculated to be between 1.0 and 1.1.

Using the methods described in Section S1.3 (Supporting Information), the detection limit (DL) is calculated by extrapolating the calibration curve and incorporating the measurement noise (refer to Figure S9b, Supporting Information)). For 500 °C, a DL between 3 and 4%RH is achieved, with the maximum just below 6%RH and the lowest just below 2%RH. At 600 °C, the DL rises to around 8%RH on average. These findings further support that the optimal annealing temperature is 500 °C. In **Table 2** we compare different sensing properties of our best sensor (annealed at 500 °C) to previously reported V_2O_5-based sensors. Hereby, our sensor stands out with the highest sensitivity of 1.427 derived from the calibration curve from measurements between 10 and 90%RH. This sensitivity is more than 330% higher than the next highest sensitivity of 0.422 observed for nanosheets.[52] Assuming the sensitivity of V_2O_5 NFs annealed at 500 °C linearly translates into the low humidity regime (1–5%RH); the

Table 2. Humidity sensing performance comparison between different V_2O_5 nanostructures.

V_2O_5 Morphology	Synthesis method	Sensitivity [%RR/%RH] [a]	Detection limit [% RH]	Response time [s]	Recovery time [s]	Refs.
Thin film	ultrasonic nebulization	0.261	Not deducible [b]	35-60	7-54	Tadeo et al. [51]
Nanosheet	hydrothermal	0.422	Not deducible [c]	240	300	Pawar et al. [52]
Nanoparticle	microwave annealing	0.357	Not deducible [d]	60 [e]	21 [e]	Charlotte and Viannie [53]
Nanobelt	O_2-assisted PVT	1.145 (1-5%RH) 0.093 (20-100%RH)	1%RH	177	341	Cho et al. [54]
Nanofiber	Electrospinning	1.427 (500 °C, max)	1.8%RH [f]	16—100 [e]	53—250 [e]	this work

[a] derived from linear regression; [b] extrapolation leads to negative detection limit value; [c] due to non-linearity; [d] due to lack of data or plot; [e] annealing temperature: 500 °C; [f] derived from linear extrapolation of the linear regression of the %RR(%RH) measurement points and considering a 3σ noise threshold.

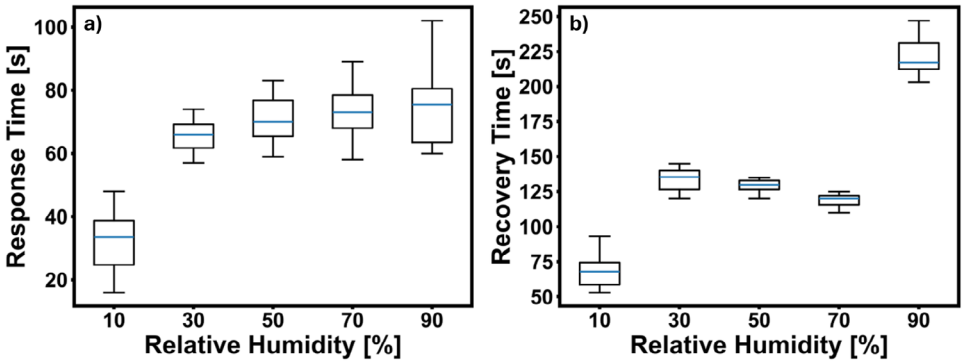

Figure 6. Response a) and recovery b) time analysis of a 16-sub-sensor chip using electrospun V_2O_5 NF annealed at 500 °C.

sensitivity even exceeds the reported 1.145 for nanobelts.[54] In contrast, the lowest projected DL of 1.8%RH is slightly above the DL reported by Cho et. al for V_2O_5 nanobelts (1%RH).[54]

The subsequent paragraph evaluates the response and recovery times, employing a conventional 90% threshold in accordance to the International Union of Pure and Applied Chemistry (IUPAC).[84] As indicated in **Figure 6**, the shortest response time, ≈16 seconds, is recorded at 10%RH. In contrast, the response times average ≈70 s for other humidity levels. Recovery times are observed to be roughly double their respective response times. The fastest recovery time of 53 s is achieved after exposure to 10%RH. However, at relative humidity levels ranging from 30%RH to 70%RH, the recovery time stabilizes at approx. 125 s. At 90%RH, the recovery time increases significantly to over 234 s on average. Comparing the response and recovery times shows that electrospun V_2O_5 NFs outperform even the fastest responding materials (thin films and nanoparticles) as shown in **Table 2.**[51,53] While the response time at higher humidity levels, and the recovery time in general, is longer in comparison. V_2O_5 NFs outperform nanosheets and nanobelts in terms of both recovery and response times.[52,54]

2.3. Sensing Properties

In this study, the electrospun vanadium pentoxide (V_2O_5) nanofibers (NFs) exhibit a positive humidity coefficient (PHC), as displayed in Figure 5. This PHC is unusual for an intrinsic n-type semiconductor. In the following, we propose two potential factors to explain the observed PHC. First, research on tungsten trioxide (WO_3) has shown that the sign of the humidity coefficient changes when the oxygen deficiency is synthetically changed.[85] A comparable interaction with titanium dioxide (TiO_2) has also been reported.[86,87] In our work, according to the XPS analysis, the derived oxygen concentration ($c_{O,pred} = 2c_{V^{4+}} + \frac{5}{2}c_{V^{5+}}$) increases and tends to approach the stoichiometric concentration with higher annealing temperatures. We here propose a similar mechanism related to oxygen deficiencies. Initially, water (H_2O) molecules adsorb on the surface, followed by proton transfer, forming a hydroxyl group at the oxygen vacancy site, as illustrated in Figure S10 (Supporting Information). The remaining hydrogen atom then forms another hydroxyl group with an adjacent V_2O_5 crystal-oxygen. The forming of surface hydroxyl groups decreases the number of oxygen-vacancy-bound electrons, which in return increases the resistance. Secondly, various literature sources indicate a PHC in various carbon allotropes.[88–92] In the XPS analysis (Figure S7, Supporting Information), carbon is also found in the V_2O_5 NF samples. Therefore, this carbon residue might chemiresistively interact with H_2O by adsorption of H_2O molecules on its surface, additionally contributing to the PHC. Moreover, electrospun V_2O_5 NFs annealed at 500 °C show negligible response to three tested gases at up to 100 ppm, as demonstrated in Figure S11 (Supporting Information), indicating favorable cross-talk sensitivity.

3. Conclusion

In this study, V_2O_5 nanofibers (NFs) were successfully synthesized by electrospinning using $VO(acac)_2$ Polyacrylonitrile

(PAN)/DMF electrolyte. The NFs were annealed at 400 to 600 °C. X-ray diffraction confirmed the formation of V_2O_5 across all temperatures, with enhanced crystallinity at higher annealing temperatures. Evident from TEM and SEM, the morphologies of the NFs transformed from hollow fibers at 400 °C to globular structures at higher temperatures. The porosity, indicated by the BET surface area, increases from 12.992 to 16.507 $m^2 g^{-1}$ as the annealing temperature is raised from 400 to 600 °C. Additionally, the V^{5+}/V^{4+} ratio increased with annealing temperature, indicating a rise in V_2O_5 concentration. These findings promote the potential of fine-tuning not only the morphology and porosity but also the chemical composition by adjusting the annealing temperature. On the application side, electrospun V_2O_5 NFs demonstrated outstanding performance in humidity sensing, particularly when annealed at 500 or 600 °C. The material demonstrated low base resistance, facilitating rapid measurement cycles, and exhibited a highly linear signal response across a relative humidity (RH) range of 10% to 90%. Furthermore, the maximum measured sensitivity at 1.427 for the NFs annealed at 500 °C outperforms all previously reported V_2O_5 materials. Analysis of response and recovery times showed humidity-dependent response and recovery times of 16–100 s, and 53–234 s, respectively. Interestingly, the V_2O_5 NFs, which is by default an intrinsic n-type semiconductor, displayed a positive humidity coefficient, potentially due to oxygen deficiencies and surface carbon. Conclusively, the findings from this study support the usage of electrospun V_2O_5 NFs as a material for high-performance humidity sensing at room temperature, combining excellent sensitivity, high signal linearity, and fast response times.

4. Experimental Section

Materials: Polyacrylonitrile (PAN, 0.3 g mL^{-1}, MW of 360000) and 0.1 g mL^{-1} $(VO(acac)_2$, 99.5%, Sigma-Aldrich, USA) were added into a mixture of DMF and ethanol (>99.8%, Sigma-Aldrich, USA). All the chemical reagents were used without further purification. After mixing, the solution was subjected to stirring for 30 h to get a homogenous solution for electrospinning.

Electrospinning of V_2O_5 Nanofibers: The electrospinning solution was put into a 10 mL glass syringe with a 200 µm steel needle. The flow rate was maintained at 2 mL h^{-1}. A working distance of 10 cm was used between the needle and the Si IDE collector was maintained at 10 kV potential. After the application of potential, the polymer jet was ejected toward the collector, fibers were extruded, and solvent vaporization occurred followed by the collection of NFs at the Si IDE collector. These electrospun fibers were then heated in the furnace at a rate of 2 °C min^{-1} to remove the adherent polymer matrices and annealed at 400, 500, and 600 °C for 15 min.

Microstructural Characterizations: X-ray diffraction (XRD, Bruker Advance D8, $\lambda = 1.5418$ Å) was used to analyze the structural phases of the V_2O_5 NF sensor. The step size (0.02°) and scan rate (2° min^{-1}) were used over a range of $2\theta = 10$ to 70°. The XRD patterns were examined using the Rietveld analysis software provided with TOPAS V3 (Bruker-AXS) inbuilt software.

SEM (FE-SEM, Hitachi 4800S, Japan) was employed to analyze the morphology of V_2O_5 NFs. The composition of V_2O_5 NF sensors was estimated using energy dispersive spectroscopy (EDS). High-resolution transmission electron microscopy (HRTEM, G20 Twin, Philips USA) was used to analyze the crystal growth at the nanoscale for samples with different annealing temperatures. The selected area diffraction (SAD) pattern was also recorded to identify the crystal planes.

The chemical states of V_2O_5 NFs were also evaluated using X-ray photoelectron spectroscopy (XPS). XPS measurements were performed using a K-Alpha+ XPS spectrometer (ThermoFisher Scientific). For data acquisition and processing, the Thermo Avantage software was used. All samples were analyzed using a microfocused, monochromated Al K_α X-ray source (400 µm spot size). The K-Alpha+ charge compensation system was employed during analysis, using 8 eV electrons and low-energy argon ions to prevent any localized charge build-up. The spectra were fitted with one or more Voigt profiles (BE uncertainty: ±0.2 eV) and Scofield sensitivity factors were applied for quantification.[55] All spectra were referenced to the C 1s peak (C—C, C—H) at 285.0 eV binding energy and verified utilizing the well-known photoelectron peaks of metallic Cu, Ag, and Au, respectively.

Humidity Measurements: A home-designed platform for chemiresistive sensors is used in this work. This platform design was previously successfully deployed in various e-nose projects.[56–64] V_2O_5 NFs are deposited on the sensing area as shown in Figure S1 (Supporting Information) (for details, refer to Section S1.1, Supporting Information). The resistances of the sub-sensors were continuously measured during an experiment with a customized read-out electronic provided by SMELLDECT GmbH. The RH variation in the range of 10–90%RH can be set by mixing dry air with fully saturated air from the bubbler at a specific ratio. The schematic of the humidity mixing system is shown in Figure S2 (Supporting Information). The sensor was used at room temperature without any excitation such as heating or UV irradiation. For the measurements in this case specifically, the discrete RH levels of 10%, 30%, 50%, 70%, and 90% were used. Furthermore, dry air at 0%RH is used for reference measurements. For analysis, the following characteristics are calculated: relative response, sensitivity, response, and recovery times. For the details of the calculations of the named quantities, refer to Section S1.3 (Supporting Information).

Supporting Information

Supporting Information is available from the Wiley Online Library or from the author.

Acknowledgements

The authors gratefully acknowledge the Deutsche Forschungsgemeinschaft (DFG, German Research Foundation) under Germany's Strategy via the Excellence Cluster 3D Matter Made to Order (3DMM2O, EXC-2082/1-390761711) for financial support.

Conflict of Interest

The authors declare no conflicts of interest

Data Availability Statement

The data that support the findings of this study are available from the corresponding author upon reasonable request.

Keywords

chemiresistor, humidity, nanofibers, sensor, vanadium pentoxide

Received: March 17, 2025
Published online: April 28, 2025

[1] H. Farahani, R. Wagiran, M. Hamidon, *Sensors.* **2014**, *14*, 7881.
[2] M. Srbinovska, C. Gavrovski, V. Dimcev, A. Krkoleva, V. Borozan, *J. Cleaner Prod.* **2015**, *88*, 297.
[3] Y.-T. Jao, P.-K. Yang, C.-M. Chiu, Y.-J. Lin, S.-W. Chen, D. Choi, Z.-H. Lin, *Nano Energy.* **2018**, *50*, 513.
[4] S. Gupta Chatterjee, S. Chatterjee, A. K. Ray, A. K. Chakraborty, *Sens. Actuators, B.* **2015**, *221*, 1170.
[5] L. Yu, Q. Zheng, H. Wang, C. Liu, X. Huang, Y. Xiao, *Anal. Chem.* **2020**, *92*, 1402.
[6] F. Bibi, C. Guillaume, N. Gontard, B. Sorli, *Trends Food Sci. Technol.* **2017**, *62*, 91.
[7] H. Yan, Z. Liu, R. Qi, *Nano Energy.* **2022**, *101*, 107591.
[8] Y. Lu, G. Yang, Y. Shen, H. Yang, K. Xu, *Nano-Micro Lett.* **2022**, *14*, 150.
[9] D. Karakaya, O. Ulucan, M. Turkan, *Int. J. Autom. Comput.* **2020**, *17*, 179.
[10] T. A. Blank, L. P. Eksperiandova, K. N. Belikov, *Sens. Actuators, B.* **2016**, *228*, 416.
[11] J.-M. Tulliani, B. Inserra, D. Ziegler, *Micromachines.* **2019**, *10*, 232.
[12] M. Jian, C. Wang, Q. Wang, H. Wang, K. Xia, Z. Yin, M. Zhang, X. Liang, Y. Zhang, *Sci. China Mater.* **2017**, *60*, 1026.
[13] B. Adhikari, S. Majumdar, *Prog. Polym. Sci.* **2004**, *29*, 699.
[14] V. Montes-García, P. Samorì, *Adv. Mater.* **2023**, 2208766.
[15] U. Mogera, A. A. Sagade, S. J. George, G. U. Kulkarni, *Sci. Rep.* **2014**, *4*, 4103.
[16] R. G. Pavelko, H. Daly, C. Hardacre, A. A. Vasiliev, E. Llobet, *Phys. Chem. Chem. Phys.* **2010**, *12*, 2639.
[17] G. Korotchenkov, V. Brynzari, S. Dmitriev, *Sens. Actuators, B.* **1999**, *54*, 197.
[18] J.-S. Kim, C. W. Na, C.-H. Kwak, H.-Y. Li, J. W. Yoon, J.-H. Kim, S.-Y. Jeong, J.-H. Lee, *ACS Appl. Mater. Interfaces.* **2019**, *11*, 25322.
[19] H. Kim, A. Haensch, I. Kim, N. Barsan, U. Weimar, J. Lee, *Adv. Funct. Mater.* **2011**, *21*, 4456.
[20] K.-I. Choi, H.-J. Kim, Y. C. Kang, J.-H. Lee, *Sens. Actuators, B.* **2014**, *194*, 371.
[21] K. Suematsu, N. Ma, M. Yuasa, T. Kida, K. Shimanoe, *RSC Adv.* **2015**, *5*, 86347.
[22] Z. Gao, G. Song, X. Zhang, Q. Li, S. Yang, T. Wang, Y. Li, L. Zhang, L. Guo, Y. Fu, *Sens. Actuators, B.* **2020**, *325*, 128810.
[23] X. Yang, W. Wang, C. Wang, H. Xie, H. Fu, X. An, X. Jiang, A. Yu, *Powder Technol.* **2018**, *339*, 408.
[24] Y. Zeng, Z. Hua, X. Tian, X. Li, Z. Qiu, C. Zhang, M. Wang, E. Li, *Sens. Actuators, B.* **2018**, *273*, 1291.
[25] Z.-A. Qiao, S.-H. Chai, K. Nelson, Z. Bi, J. Chen, S. M. Mahurin, X. Zhu, S. Dai, *Nat. Commun.* **2014**, *5*, 3705.
[26] M. Yao, W. Tang, G. Wang, B. Nath, G. Xu, *Adv. Mater.* **2016**, *28*, 5229.
[27] L. Zhang, Y. Zhou, S. Han, *Angew. Chem., Int. Ed.* **2021**, *60*, 15192.
[28] S. Liang, X. He, F. Wang, W. Geng, X. Fu, J. Ren, X. Jiang, *Sens. Actuators, B.* **2015**, *208*, 363.
[29] Q. Kuang, C. Lao, Z. L. Wang, Z. Xie, L. Zheng, *J. Am. Chem. Soc.* **2007**, *129*, 6070.
[30] C. Zhang, X. Geng, H. Liao, C.-J. Li, M. Debliquy, *Sens. Actuators, B.* **2017**, *242*, 102.
[31] J. Ding, Z. Zheng, Z. Song, S. Ding, J. Wen, K. Liu, C. Zhang, H. Li, *Mater. Des.* **2023**, *234*, 112360.
[32] G. Korotcenkov, *Nanomaterials.* **2021**, *11*, 1544.
[33] R. Shaik, R. K. Kampara, A. Kumar, C. S. Sharma, M. Kumar, *Coord. Chem. Rev.* **2022**, *471*, 214752.
[34] E. Comini, G. Faglia, G. Sberveglieri, Z. Pan, Z. L. Wang, *Appl. Phys. Lett.* **2002**, *81*, 1869.
[35] C. Li, D. Zhang, X. Liu, S. Han, T. Tang, J. Han, C. Zhou, *Appl. Phys. Lett.* **2003**, *82*, 1613.
[36] G. T. Chandrappa, N. Steunou, S. Cassaignon, C. Bauvais, J. Livage, *Catal. Today.* **2003**, *78*, 85.
[37] J. Livage, *Chem. Mater.* **1991**, *3*, 578.
[38] Y. Wang, G. Cao, *Chem. Mater.* **2006**, *18*, 2787.
[39] D. Meng, J. Si, M. Wang, G. Wang, Y. Shen, X. San, F. Meng, *Chin. Chem. Lett.* **2020**, *31*, 2133.
[40] T. K. Le, M. Kang, S. W. Kim, *Ceram. Int.* **2019**, *45*, 15781.
[41] A. A. Akl, *J. Phys. Chem. Solids.* **2010**, *71*, 223.
[42] W. Wu, Y. Wang, X. Wang, Q. Chen, X. Wang, S. Yang, X. Liu, J. Guo, Z. Yang, *ChemInform.* **2010**, *41*, chin201005009.
[43] A. Subrahmanyam, Y. Bharat Kumar Redd, C. L. Nagendra, *J. Phys. D: Appl. Phys.* **2008**, *41*, 195108.
[44] Y. Wei, M. Li, J. Zheng, C. Xu, *Thin Solid Films.* **2013**, *534*, 446.
[45] J. Xia, C. Yuan, S. Yanagida, *ACS Appl. Mater. Interfaces.* **2010**, *2*, 2136.
[46] X. Zhao, Y. Yan, L. Mao, M. Fu, H. Zhao, L. Sun, Y. Xiao, G. Dong, *RSC Adv.* **2018**, *8*, 31081.
[47] J. Muster, G. T. Kim, V. Krstić, J. G. Park, Y. W. Park, S. Roth, M. Burghard, *Adv. Mater.* **2000**, *12*, 420.
[48] Q. Zhang, Z. Pang, W. Hu, J. Li, Y. Liu, Y. Liu, F. Yu, C. Zhang, M. Xu, *Appl. Surf. Sci.* **2021**, *541*, 148418.
[49] B. Sharma, A. Sharma, J.-S. Kim, *Sens. Actuators, B.* **2018**, *262*, 758.
[50] H. Wang, J. Bai, M. Dai, K. Liu, Y. Liu, L. Zhou, F. Liu, F. Liu, Y. Gao, X. Yan, L. Geyu, *Sens. Actuators, B.* **2020**, *304*, 127287.
[51] I. J. Tadeo, R. Parasuraman, S. B. Krupanidhi, A. M. Umarji, *Nano Express.* **2020**, *1*, 010005.
[52] M. S. Pawar, P. K. Bankar, M. A. More, D. J. Late, *RSC Adv.* **2015**, *5*, 88796.
[53] M. R. Charlotte, L. R. Viannie, *J. Mater. Sci.* **2024**, *59*, 22034.
[54] S. Cho, S. H. Lim, J. Oh, T.-S. Ju, S. Yang, H. H. Kim, Y. Kim, *Sens. Actuators, B.* **2025**, *423*, 136711.
[55] J. H. Scofield, *J. Electron Spectrosc. Relat. Phenom.* **1976**, *8*, 129.
[56] I. Kiselev, M. Sommer, J. Kaur Mann, V. V. Sysoev, *IEEE Sensors J.* **2010**, *10*, 849.
[57] V. V. Sysoev, I. Kiselev, M. Frietsch, J. Goschnick, *Sensors.* **2004**, *4*, 37.
[58] V. Yu Musatov, V. V. Sysoev, M. Sommer, I. Kiselev, M. Pardo, G. Sberveglieri, *AIP Conference Proceedings*, AIP, Brescia Italy **2009**, pp. 469–472.
[59] C. Arnold, M. Harms, J. Goschnick, *IEEE Sensors J.* **2002**, *2*, 179.
[60] C. Arnold, D. Haeringer, I. Kiselev, J. Goschnick, *Sens. Actuators, B.* **2006**, *116*, 90.
[61] J. Goschnick, I. Koronczi, M. Frietsch, I. Kiselev, *Sens. Actuators, B.* **2005**, *106*, 182.
[62] V. V. Sysoev, I. Kiselev, T. Schneider, M. Bruns, M. Sommer, W. Habicht, V. Yu Musatov, E. Strelcov, A. Kolmakov, M. Pardo, G. Sberveglieri, *AIP Conference Proceedings*, AIP, Brescia Italy **2009**, pp. 403–404.
[63] C. Arnold, W. Andlauer, D. Haringer, R. Korber, J. Goschnick, *Proceedings of IEEE Sensors*, IEEE, Orlando, FL, USA **2002**, p. 426.
[64] V. V. Sysoev, V. Yu Musatov, A. A. Maschenko, A. S. Varegnikov, A. A. Chrizostomov, I. Kiselev, T. Schneider, M. Bruns, M. Sommer, M. Pardo, G. Sberveglieri, *AIP Conference Proceedings*, AIP, Brescia Italy **2009**, pp. 539–542.
[65] K.-Y. Pan, D.-H. Wei, *Nanomaterials.* **2016**, *6*, 140.
[66] A. Jain, S. R. Manippady, R. Tang, H. Nishihara, K. Sobczak, V. Matejka, M. Michalska, *Sci. Rep.* **2022**, *12*, 21024.
[67] M. M. Margoni, S. Mathuri, K. Ramamurthi, R. R. Babu, K. Sethuraman, *Thin Solid Films.* **2016**, *606*, 51.
[68] Y. Vijayakumar, K. N. Reddy, A. V. Moholkar, *Mater. Tehnol.* **2015**, *49*, 371.
[69] A. Monshi, M. R. Foroughi, M. R. Monshi, *World J. Nano Sci. Eng.* **2012**, *02*, 154.
[70] J. I. Langford, A. J. C. Wilson, *J. Appl. Crystallogr.* **1978**, *11*, 102.
[71] A. Isotherms, In *Gas Adsorption Equilibria*, Kluwer Academic Publishers, Boston **2005**, pp. 359–413.
[72] H. Liu, P. He, Z. Li, D. Sun, H. Huang, J. Li, G. Zhu, *Chem.-Asian J.* **2006**, *1*, 701.

[73] P. K. Johnston, E. Doyle, R. A. Orzel, *J. Am. Coll. Toxicol.* **1988**, *7*, 139.
[74] G. Wee, H. Z. Soh, Y. L. Cheah, S. G. Mhaisalkar, M. Srinivasan, *J. Mater. Chem.* **2010**, *20*, 6720.
[75] M. C. Biesinger, B. P. Payne, A. P. Grosvenor, L. W. M. Lau, A. R. Gerson, R. St C Smart, *Appl. Surf. Sci.* **2011**, *257*, 2717.
[76] J. Mendialdua, R. Casanova, Y. Barbaux, *J. Electron Spectrosc. Relat. Phenom.* **1995**, *71*, 249.
[77] G. Silversmit, D. Depla, H. Poelman, G. B. Marin, R. De Gryse, *Surf. Sci.* **2006**, *600*, 3512.
[78] K. M. Koczkur, S. Mourdikoudis, L. Polavarapu, S. E. Skrabalak, *Dalton Trans.* **2015**, *44*, 17883.
[79] Z. Strassberger, E. V. Ramos-Fernandez, A. Boonstra, R. Jorna, S. Tanase, G. Rothenberg, *Dalton Trans.* **2013**, *42*, 5546.
[80] T. J. Frankcombe, Y. Liu, *Chem. Mater.* **2023**, *35*, 5468.
[81] H. Idriss, *Surf. Sci.* **2021**, *712*, 121894.
[82] R. Berenguer, M. O. Guerrero-Pérez, I. Guzmán, J. Rodríguez-Mirasol, T. Cordero, *ACS Omega.* **2017**, *2*, 7739.
[83] V. Mounasamy, G. K. Mani, S. Madanagurusamy, *Microchim. Acta.* **2020**, *187*, 253.
[84] J. G. Calvert, *Pure Appl. Chem.* **1990**, *62*, 2167.
[85] J. Qian, Z. Peng, Z. Shen, Z. Zhao, G. Zhang, X. Fu, *Sci. Rep.* **2016**, *6*, 25574.
[86] R. Schaub, P. Thostrup, N. Lopez, E. Lægsgaard, I. Stensgaard, J. K. Nørskov, F. Besenbacher, *Phys. Rev. Lett.* **2001**, *87*, 266104.
[87] S. Wendt, R. Schaub, J. Matthiesen, E. K. Vestergaard, E. Wahlström, M. D. Rasmussen, P. Thostrup, L. M. Molina, E. Lægsgaard, I. Stensgaard, B. Hammer, F. Besenbacher, *Surf. Sci.* **2005**, *598*, 226.
[88] S. Tachibana, Y.-F. Wang, T. Sekine, Y. Takeda, J. Hong, A. Yoshida, M. Abe, R. Miura, Y. Watanabe, D. Kumaki, S. Tokito, *ACS Appl. Mater. Interfaces.* **2022**, *14*, 5721.
[89] A. Mansoori, S. Ahmad, S. Bansal, M. Vashishath, *ECS Sens. Plus.* **2022**, *1*, 044401.
[90] A. Yoshida, Y.-F. Wang, S. Tachibana, A. Hasegawa, T. Sekine, Y. Takeda, J. Hong, D. Kumaki, T. Shiba, S. Tokito, *Carbon Trends.* **2022**, *7*, 100166.
[91] B. Zhao, V. S. Sivasankar, S. K. Subudhi, A. Dasgupta, S. Das, *ACS Appl. Nano Mater.* **2023**, *6*, 1459.
[92] Z.-H. Duan, Q.-N. Zhao, C.-Z. Li, S. Wang, Y.-D. Jiang, Y.-J. Zhang, B.-H. Liu, H.-L. Tai, *Rare Met.* **2021**, *40*, 1762.